AstroSat observation of the accreting millisecond X-ray pulsar SAX J1808.4–3658 during its 2019 outburst

Rahul Sharma [ORCID],[1,2]★ Andrea Sanna [ORCID][3] and Aru Beri [ORCID][2,4]

[1]*Raman Research Institute, C.V. Raman Avenue, Sadashivanagar, Bengaluru, Karnataka 560080, India*
[2]*Indian Institute of Science Education and Research (IISER) Mohali, Punjab 140306, India*
[3]*Universitá degli Studi di Cagliari, Dipartimento di Fisica, SP Monserrato-Sestu, KM 0.7, 09042 Monserrato, Italy*
[4]*School of Physics and Astronomy, University of Southampton, Southampton, Hampshire, SO17 1BJ, United Kingdom*

ABSTRACT

We report on the analysis of the *AstroSat* data set of the accreting millisecond X-ray pulsar SAX J1808.4–3658, obtained during its 2019 outburst. We found coherent pulsations at ∼401 Hz and an orbital solution consistent with previous studies. The 3–20 keV pulse profile can be well fitted with three harmonically related sinusoidal components with background-corrected fractional amplitudes of ∼ 3.5 per cent, ∼ 1.2 per cent and ∼ 0.37 per cent for the fundamental, second and third harmonics, respectively. Our energy-resolved pulse profile evolution study indicates a strong energy dependence. We also observed a soft lag in the fundamental and hard lags during its harmonic. The broad-band spectrum of SAX J1808.4–3658 can be described well using a combination of the thermal emission component with $kT \sim 1$ keV, a thermal Comptonization ($\Gamma \sim 1.67$) from the hot corona and broad emission lines due to Fe.

Key words: accretion, accretion discs – stars: neutron – X-ray: binaries – X-rays: individual: SAX J1808.4–3658.

1 INTRODUCTION

SAX J1808.4–3658 was the first X-ray binary to show millisecond X-ray pulsations at ∼401 Hz in a ∼2 h compact binary orbit (Wijnands & van der Klis 1998a; Chakrabarty & Morgan 1998). Since then, 25 such sources with millisecond pulsations have been discovered (e.g. Di Salvo & Sanna 2020; Ng et al. 2021; Bult et al. 2022; Sanna et al. 2022b). These systems are generally referred as accretion-powered millisecond X-ray pulsars (AMXPs; for reviews, see, e.g. Patruno & Watts 2012; Campana & Di Salvo 2018; Di Salvo & Sanna 2020). These systems are transient in nature and can be observed during outburst phases. AMXPs are a subclass of low-mass X-ray binaries (LMXBs; Charles 2011) where the companion's mass is $\lesssim 1\,M_\odot$.

The magnetic fields of AMXPs have been estimated to be of the order of $\sim 10^8 - 10^9$ G (see, e.g. Cackett et al. 2009; Mukherjee et al. 2015; Ludlam et al. 2017; Pan et al. 2018; Sharma et al. 2020; Beri et al. submitted), strong enough to channel at least part of the accretion stream to the magnetic poles, which results in X-ray modulation at neutron star (NS) spin. The X-ray spectrum of AMXPs can be modelled using thermal emission from an accretion disc and/or NS surface, thermal Comptonization, and reprocessed emission from the accretion disc in the form of reflection spectrum (e.g. Cackett et al. 2009, 2010; Papitto et al. 2009, 2010, 2013; Pintore et al. 2016; Di Salvo et al. 2019; Sharma, Jain & Dutta 2019). They mostly show the hard spectral state with some exceptions (Sharma et al. 2019; Di Salvo & Sanna 2020, Beri et al. submitted) that show the spectral state transition between the hard and soft spectral states similar to atoll sources (e.g. Hasinger & van der Klis 1989).

Since 1996, SAX J1808.4–3658 has been frequently observed in outburst every 2.5–4 yr. A total of 10 outbursts (in 1996, 1998, 2000, 2002, 2005, 2008, 2011, 2015, 2019 and 2022) have been observed. Over the last two decades, SAX J1808.4–3658 has been studied extensively. Aspects of coherent pulsations (Poutanen & Gierliński 2003; Jain, Dutta & Paul 2007; Hartman et al. 2008; Burderi et al. 2009; Patruno et al. 2017; Sanna et al. 2017; Bult et al. 2020), spectral characteristics (Gierliński, Done & Barret 2002; Cackett et al. 2009; Papitto et al. 2009; Di Salvo et al. 2019), thermonuclear X-ray bursts (in 't Zand et al. 1998; Galloway & Cumming 2006; Bhattacharyya & Strohmayer 2007; Bult et al. 2019a) and aperiodic and quasi-periodic variability (Wijnands & van der Klis 1998b; Wijnands et al. 2003; van Straaten, van der Klis & Wijnands 2005; Patruno et al. 2009c; Bult & van der Klis 2015) have been investigated in depth. The properties of the source have also been investigated thoroughly during quiescence and outburst in multiwavelength studies (e.g. radio, optical, ultraviolet, etc.; Gaensler, Stappers & Getts 1999; Wang et al. 2001, 2013; Cornelisse et al. 2009; Heinke et al. 2009; Patruno et al. 2017; Tudor et al. 2017; Baglio et al. 2020; Goodwin et al. 2020; Ambrosino et al. 2021).

The 2019 outburst of SAX J1808.4–3658 started around 2019 August 6 (Bult et al. 2019b; Goodwin et al. 2019; Parikh & Wijnands 2019) and lasted about a month. After episodes of reflaring, the source went back into a quiescence state (Baglio, Russell & Lewis 2019a; Baglio et al. 2019b; Bult et al. 2019c), similar to its previous outbursts (Patruno et al. 2016). Enhancement in the optical flux was observed 12 d before the onset of outburst, (Russell et al. 2019; Goodwin et al. 2020). The Neutron Star Interior Composition Explorer (NICER; Gendreau & Arzoumanian 2017) monitored the 2019 outburst from the start to the reflaring states. Bult et al. (2020) performed a coherent timing analysis using NICER observations during the outburst of 2019, and found a secular spin-down of the pulsar at rate of 1.01(7) ×

★ E-mail: rahul1607kumar@gmail.com, rsharma@rri.res.in
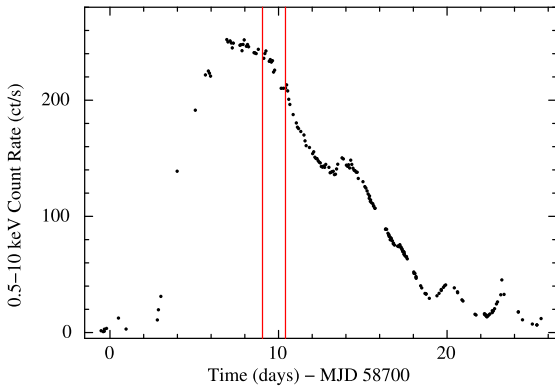
Figure 1. The 0.5–10 keV NICER light curve of SAX J1808.4–3658 during its 2019 outburst. The two vertical red lines represent the time range of the *AstroSat* observation.

10^{-15} Hz s^{-1}. A very bright photospheric radius expansion (PRE) burst was also observed with NICER (Bult et al. 2019a). Coherent pulsations in optical and ultraviolet were detected at ∼401 Hz, likely to be driven by synchro-curvature radiation in the pulsar magnetosphere or just outside it (Ambrosino et al. 2021). Recently, SAX J1808.4–3658 was again observed in outburst in 2022 August (Sanna et al. 2022c).

During the 2019 outburst, we also observed SAX J1808.4–3658 with the *AstroSat* mission under Target of Opportunity (ToO). According to NICER observations, the outburst reached its peak on 2019 August 13 (MJD 58708), after which it started to decay (Bult et al. 2019c). The *AstroSat* observation was carried out just after the peak of the outburst (see Fig. 1). In this work, we report for the first time the results from the timing analysis carried out using the *AstroSat*/Large Area X-ray Proportional Counter (LAXPC) data and the spectroscopy performed using Soft X-ray Telescope (SXT) and LAXPC data.

2 OBSERVATIONS AND DATA ANALYSIS

AstroSat is India's first dedicated multiwavelength astronomy satellite (Agrawal 2006; Singh et al. 2014), launched in 2015. It has five principal payloads onboard: (i) the SXT; (ii) the LAXPC; (iii) the Cadmium–Zinc–Telluride Imager (CZTI); (iv) the Ultraviolet Imaging Telescope (UVIT); and (v) the Scanning Sky Monitor (SSM). Table 1 gives the log of observations that have been used in this work. We analysed data from the SXT and LAXPC only.

2.1 *AstroSat*/LAXPC

The LAXPC is one of the primary instruments onboard *AstroSat*. It consists of three co-aligned identical proportional counters (LAXPC10, LAXPC20 and LAXPC30) that work in the energy range of 3–80 keV. Each LAXPC detector independently records the arrival time of each photon with a time resolution of 10 μs and has five layers (for details, see Yadav et al. 2016; Antia et al. 2017).

As LAXPC10 was operating at low gain and detector LAXPC30[1] was switched off during the observation, we used only the LAXPC20 detector for our analysis. We used the data collected in the Event

Analysis (EA) mode and processed using the LAXPCSOFT[2] version 3.1.1 software package to extract light curves and spectra. LAXPC detectors have dead-time of 42 μs and the extracted products are dead-time corrected. The background in the LAXPC is estimated from the blank sky observations (for details, see Antia et al. 2017). To minimize the background, we have performed all analysis using the data from the top layer (L1, L2) of the LAXPC20 detector. We have used corresponding response files to obtain channel-to-energy conversion information while performing energy-resolved analysis.

We corrected the LAXPC photon arrival times to the Solar system barycentre by using the AS1BARY[3] tool. We used the best available position of the source, RA (J2000) = $18^h08^m27^s.647$ and Dec. (J2000) = $-36°58'43''.90$ obtained through pulsar timing astrometry (Bult et al. 2020).

2.2 *AstroSat*/SXT

The Soft X-ray Telescope (SXT) is a focusing X-ray telescope with a CCD in the focal plane that can perform X-ray imaging and spectroscopy in the 0.3–7 keV energy range (Singh et al. 2016, 2017). SAX J1808.4–3658 was observed in the Photon Counting (PC) mode with the SXT (Table 1). Level 1 data were processed with AS1SXTLevel2-1.4b pipeline software to produce level 2 clean event files. The level 2 cleaned files from each orbit were merged using the SXT Event Merger Tool (Julia Code). This merged event file was then used to extract the image, light curves and spectra using the FTOOL task XSELECT, provided as part of HEASOFT version 6.29. A circular region with a radius of 15 arcmin centred on the source was used. For spectral analysis, we have used the the blank sky SXT spectrum as background (SkyBkg_comb_EL3p5_Cl_Rd16p0_v01.pha) and the spectral redistribution matrix file (sxt_pc_mat_g0to12.rmf) provided by the SXT team.[4] We generated the correct off-axis auxiliary response files (ARFs) using the sxtARFModule tool from the on-axis ARF (sxt_pc_excl00_v04_20190608.arf) provided by the SXT instrument team.

3 RESULTS

3.1 Light curve

Fig. 1 shows the light curve of SAX J1808.4–3658 during its 2019 outburst, as observed with NICER. The *AstroSat* observation (red vertical lines) was carried out near the peak of the outburst. Fig. 2 shows the background-corrected light curve extracted from LAXPC20 binned at 100 s in two different energy bands: 3–10 keV (top panel) and 10–30 keV (middle panel). The LAXPC light curves show the persistent emission separated by data gaps due to Earth's occultation and the South Atlantic Anomaly (SAA) passage. No type I X-ray burst was observed during the observation. The bottom panel presents the hardness ratio calculated using light curves in the two energy bands, 3–10 and 10–30 keV. As the hardness ratio is observed to be constant during the observation, this suggests that the source did not seem to change spectral state within the observation duration.

[1]LAXPC30 has been switched off since 2018 March 8 due to abnormal gain changes (see http://astrosat-ssc.iucaa.in/).

Table 1. Log of X-ray observations.

Instrument	OBS ID	Start time (YY-MM-DD HH:MM:SS)	MJD	Stop time (YY-MM-DD HH:MM:SS)	MJD	Mode	Obs span (ks)
AstroSat/LAXPC	9000003090	2019-08-14 01:10:46	58709.04914	2019-08-15 09:56:53	58710.41450	EA	118
AstroSat/SXT	9000003090	2019-08-14 02:19:02	58709.09655	2019-08-15 10:30:16	58710.43768	PC	116
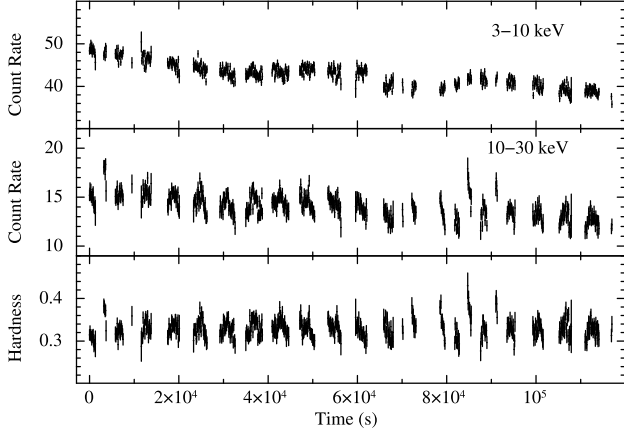
Figure 2. The top two panels show background-corrected light curves from LAXPC20 binned at 100 s in energy ranges of 3–10 and 10–30 keV, respectively. The bottom panel shows the hardness ratio (= 10–30 keV/3–10 keV) binned at 100 s.

3.2 Aperiodic timing

We created the power density spectrum (PDS) using the LAXPC20 event data set in the 3–20 keV energy range. We binned the data at 0.5 ms to have a Nyquist frequency of 1000 Hz and used ~262-s segments to calculate the Fourier transform. All power spectra were averaged and rebinned geometrically with a factor of 1.05. No background correction was applied. The power spectra were calculated using rms normalization and Poisson noise was subtracted using the FTOOL powspec norm = -2. The PDS of X-ray binaries can be described in terms of a sum of Lorentzian functions (e.g. Nowak 2000; Belloni, Psaltis & van der Klis 2002). The Lorentzian profile is a function of frequency and can be defined as

$$P(\nu) = \frac{r^2 \Delta}{2\pi} \frac{1}{(\nu - \nu_0)^2 + (\Delta/2)^2}, \qquad (1)$$

where ν_0 is the centroid frequency, Δ is the full width at half-maximum (FWHM), and r is the integrated fractional rms. The quality factor of Lorentzian $Q = \nu_0/\Delta$ is used to differentiate whether a feature is a quasi-periodic oscillation (QPO) or noise. The components with $Q > 2$ are generally considered to be QPOs, or otherwise band-limited noise (e.g. Belloni et al. 2002; van der Klis 2004; Bult & van der Klis 2015).

SAX J1808.4–3658 is known to show peaked noise, low-frequency QPOs and kHz QPOs (e.g. Wijnands & van der Klis 1998b; Wijnands et al. 2003; van Straaten et al. 2005; Patruno et al. 2009c; Bult & van der Klis 2015). Fig. 3 shows the PDS of SAX J1808.4–3658 from LAXPC20 in 0.004–200 Hz, as no significant power is observed above 200 Hz. It shows only the red noise and no low-frequency QPO was observed. The PDS can be well modelled with a combination of three Lorentzian functions (see Table 2). Generally, each Lorentzian of the noise component can be expressed with characteristic frequency $\nu_{max} = \sqrt{\nu_0^2 + (\Delta/2)^2}$ and fractional rms
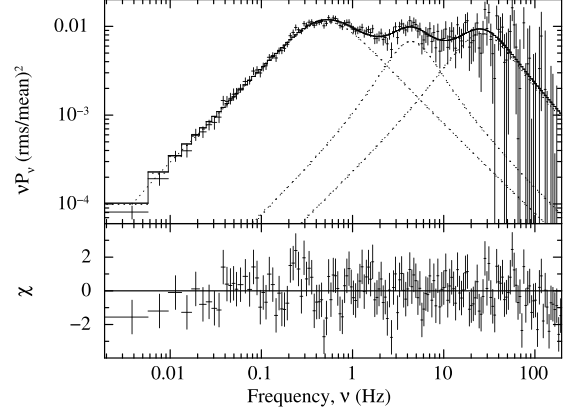
Figure 3. PDS of SAX J1808.4–3658 in the 3–20 keV energy range. The PDS is rms normalized and white noise is subtracted. Three Lorentzian functions are used to model the PDS in the range 0.004–200 Hz.

Table 2. The best fit of the PDS. Reported errors are at 1σ confidence level for a single parameter.

Component	1	2	3
Frequency, ν_0 (Hz)	$0.1675^{+0.015}_{-0.016}$	$3.33^{+0.37}_{-0.74}$	$17.1^{+5.6}_{-6.3}$
FWHM, Δ (Hz)	0.96 ± 0.05	$5.7^{+2.1}_{-1.5}$	$39.6^{+7.2}_{-6.4}$
Characteristic frequency, ν_{max} (Hz)	0.508	4.38	26.16
rms (%)	$17.5^{+0.3}_{-0.4}$	$11.0^{+1.8}_{-1.4}$	13.2 ± 1.2
χ^2/degrees of freedom (d.o.f.)		175/151	

amplitude (Belloni et al. 2002; Bult & van der Klis 2015). We found $\nu_{max} = $ ~0.5, 4.4 and 26 Hz and rms = ~17.5, 11 and 13 per cent for the three Lorentzians, respectively.

3.3 Coherent timing analysis

The pulses from a rotating NS can lose coherence within a relatively short time-scale due to Doppler modulations of the arrival time of pulses in a short orbital period of ~2 h. In addition, the small pulse fraction can also make it difficult to detect pulse arrival times from small segments of the light curve. Therefore, to detect the pulsations or true spin frequency during these observations, the light curve should be corrected for the binary motion. So, we corrected the photon time of arrivals of the *AstroSat*/LAXPC data set for the delays caused by the binary motion. The delay induced by the orbital motion can be written as (Burderi et al. 2007)

$$\frac{z(t)}{c} = \frac{a_x \sin i}{c} \sin \left[\frac{2\pi}{P_{orb}} (t - T^\star) \right], \qquad (2)$$

where $a_x \sin i/c$ is the projected semimajor axis of the NS orbit in light seconds, P_{orb} is the orbital period, and $T^\star$ is the time of passage from the ascending node.

Table 3. Timing solution of SAX J1808.4–3658 during the outburst of 2019. Errors are at the 1σ confidence level.

Parameter	Case 1	Case 2
Spin frequency, ν (Hz)	400.97521014(21)	400.97521004(26)
Spin frequency derivative, $\dot{\nu}$ (Hz s^{-1})	$1.1(1.7) \times 10^{-11}$	$1.8(1.9) \times 10^{-11}$
Ascending node passage, $T^\star$ (MJD)	58715.0221031[a]	58715.02212 (7)
Orbital period, P_{orb} (s)	7249.1552[a]	7249.16 (10)
Projected semimajor axis, $a_x \sin i/c$ (lt-ms)	62.8091[a]	62.83 (3)
Eccentricity, e		0[a]
Reference epoch, T_0 (MJD)		58709.74
χ^2/d.o.f.	46/31	41/28

[a] Taken from Bult et al. (2020).

Bult et al. (2020) found the latest updated orbital solution at the outburst of 2019 using NICER observations. Therefore, we corrected photon time of arrivals by adopting the 2019 orbital ephemeris reported by Bult et al. (2020). We then applied epoch-folding techniques to search for X-ray pulsation around the spin frequency value $\nu_0 = 400.97520983$ Hz, corresponding to the spin frequency measured during the same outburst with NICER (Bult et al. 2020). We used 16 phase bins to sample the signal. We explored the frequency space with steps of 10^{-8} Hz for a total of 10 001 steps. The most significant pulse profile was been obtained for an average local spin frequency of $\bar{\nu} = 400.97520994$ Hz.

We also investigated the evolution of the pulse phase delays. We divided the data in time intervals of $\sim$500 s and epoch-folded each segment in eight phase bins at the mean spin frequency $\bar{\nu}$ with respect to the epoch $T_0 = 58709.74$ MJD. We modelled each pulse profile with a sinusoidal function for the fundamental component to determine the corresponding sinusoidal amplitude and the phase delay. We selected only folded profiles with the ratio between the sinusoidal amplitude and the corresponding 1σ error larger than 3. The fractional amplitude (non-background corrected) of the fundamental varies between $\sim$2.2−3.7 per cent.

We modelled the time evolution of the pulse phase delays obtained from the fundamental component with the following model (see, e.g. Burderi et al. 2007; Sanna et al. 2020, 2022a):

$$\Delta\phi(t) = \phi_0 + \Delta\nu_0(t - T_0) - \frac{1}{2}\dot{\nu}(t - T_0)^2 + R_{orb}(t). \quad (3)$$

Here, $\Delta\nu_0 = (\nu_0 - \bar{\nu})$ is the spin frequency correction and $\dot{\nu}$ is the spin frequency derivative, estimated with respect to the reference epoch T_0. $R_{orb}(t)$ models the differential correction to the ephemeris used to generate the pulse phase delays (see, e.g. Deeter, Boynton & Pravdo 1981). As the orbital solution is already updated at the 2019 outburst, we set $R_{orb}(t) = 0$ (case 1) and measured the updated spin frequency and its derivative. As a second case, we also allowed $R_{orb}(t)$ and measured the orbital parameters along with spin frequency and its derivative. Best-fitting parameters are reported in Table 3. Fig. 4 shows the residuals obtained after the best-fitting parameters are subtracted from the phase delays; black points represent quadratic only, while red points denote quadratic + orbital. The obtained best-fitting frequency is consistent with the spin frequency observed with NICER (Bult et al. 2020). We obtained a 3σ upper limit on the spin frequency derivative of -4×10^{-11} Hz s^{-1} to 6.2×10^{-11} Hz s^{-1} for case 1 and -3.9×10^{-11} Hz s^{-1} to 7.5×10^{-11} Hz s^{-1} for case 2. The obtained orbital solution is also consistent with the solution of Bult et al. (2020) within the errors.

Fig. 5 presents the best pulse profile obtained by epoch-folding the LAXPC data set at $\bar{\nu}$ and sampling the signal in 16 phase bins in the energy range of 3–20 keV. The pulse shape is well fitted with
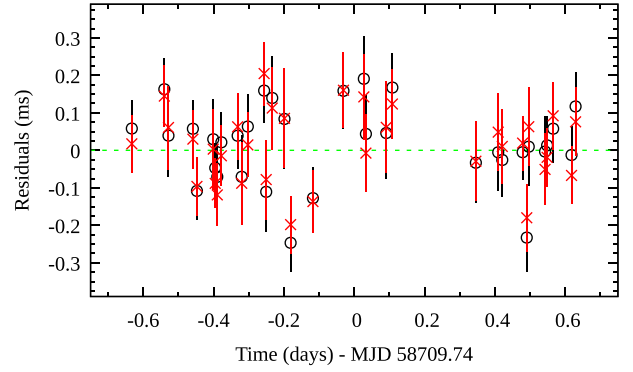
Figure 4. The residuals obtained from fitting the pulse phase delays of the fundamental component. Red crosses represent the residuals with equation (3) (quadratic + orbital) and black circles represent the residuals with only quadratic function, $R_{orb}(t) = 0$.
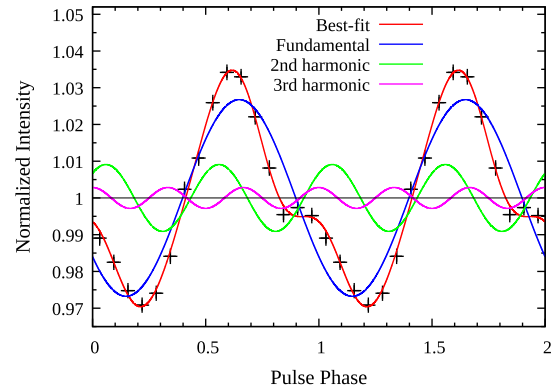
Figure 5. The average pulse profile (black points) of SAX J1808.4–3658 obtained by epoch-folding the *AstroSat*/LAXPC data with $\bar{\nu}$ in the energy range 3–20 keV after correcting for the orbital solution. The epoch used was $T_0 = 58709.74$ MJD. The best-fitting model (red solid line) is the superposition of three sinusoidal functions with harmonically related periods. The fundamental, second and third harmonic components are presented by the blue, green and magenta dashed lines, respectively. For clarity, we show two cycles of the pulse profile.

three harmonically related sinusoidal functions with background-corrected fractional amplitudes of 3.54(7) per cent, 1.21(7) per cent and 0.37(7) per cent for the fundamental, second and third harmonics, respectively.

We also checked for the energy dependence of the pulse amplitude and phase. We divided the whole data set depending on the different energy range and epoch-folded each with $\bar{\nu}$. Some of the energy-resolved pulse profiles are presented in Fig. A1. Each folded pulse profile was then fitted with two harmonically related sinusoidal functions (the third harmonic was not detected in the energy-resolved pulse profiles, likely because of poor statistics of the selected intervals). Fig. 6 (top panel) shows the variation of the background-corrected fractional amplitude of the fundamental (black points) and harmonic (grey points) components of the pulse. The fractional amplitude of the fundamental was found to be $\sim$5 per cent in the 3–5 keV energy range, and above 5 keV a constant decrease was observed with energy. While the harmonic component increased with energy. Fig. 6 (bottom panel) shows the time lag (calculated from the phase lag) of the fundamental and harmonic components of the pulse with energy. The zero lag value corresponds to the phase of
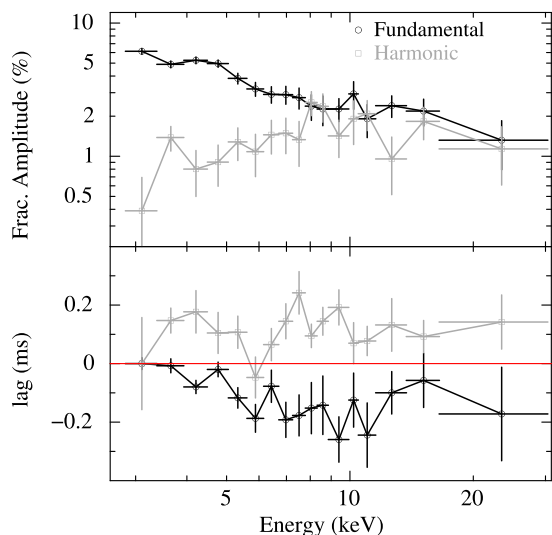
Figure 6. Top panel: the energy dependence of the pulse fractional amplitude for the fundamental and harmonic components. Bottom panel: the observed time lag of the fundamental and harmonic components of the pulse with energy. The zero lag corresponds to the phase of the pulse profile in 2.83–3.38 keV (channel 5 of LAXPC20 corresponding to 3 keV).

the pulse profile in the energy band of 2.83−3.38 keV. It shows a negative time lag (i.e. high-energy emission is coming earlier than the softer emission) of 0.1–0.2 ms for the fundamental component at higher energies (above 5 keV) while the harmonic component shows a positive lag of similar order. By comparing the top and bottom plots of Fig. 6, the phase lags seem to become specular as soon as the fractional amplitude of the two components reaches similar values (above ∼7 keV).

3.4 Broad-band spectral analysis

We modelled the SXT (0.3–7 keV) and LAXPC (3–25 keV[5]) spectra simultaneously. Both spectra were grouped using GRPPHA to have a minimum count of 20 counts per bin. An inter-instrumental calibration constant was added, which was fixed to 1 for the LAXPC and allowed to vary for the SXT. We also allowed the gain of response matrix for the SXT to vary, with the slope fixed at 1. A gain offset of ∼34 eV was obtained. A systematic uncertainty of 2 per cent was also introduced during the spectral fitting (Antia et al. 2017; Sharma et al. 2020). We used XSPEC (Arnaud 1996) for the spectral fitting with the component tbabs to model interstellar neutral hydrogen absorption (Wilms, Allen & McCray 2000).

To model the broad-band spectrum, we first started with the absorbed thermal Comptonized emission model, nthcomp (Zdziarski, Johnson & Magdziarz 1996; Życki, Done & Smith 1999). The nthcomp model shows that the hot electrons Compton up-scatter the seed photons originating from the NS surface/boundary layer or inner accretion disc. Using the parameter *inp_type*, the input seed type can be selected. During all fittings, the electron temperature was unconstrained so we fixed it at a reasonable value of 100 keV. The obtained fit with tbabs×nthcomp was unacceptable with both input seed photon types (χ^2/d.o.f. ∼ 1133/583).

We then added a thermal component in the form of a single-temperature blackbody. It did not provide a satisfactory fit

[5]Above 25 keV, LAXPC20 showed systematic residuals (Sharma et al. 2023).
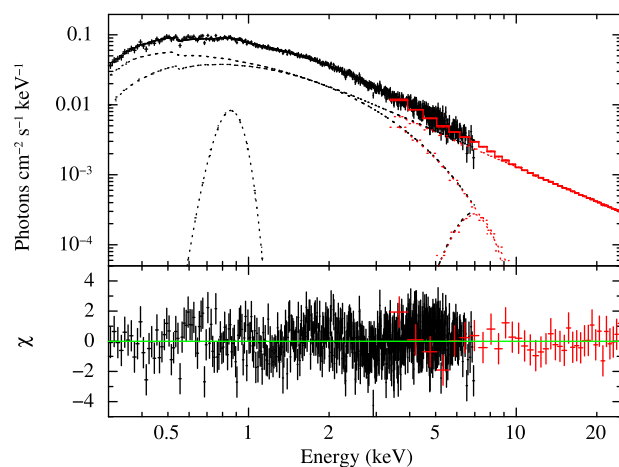
Figure 7. Broad-band spectrum of SAX J1808.4–3658 from the SXT and the LAXPC instrument fitted simultaneously with the best-fitting model tbabs*(diskbb+nthcomp+gaussian+gaussian). The lower panel shows residuals, χ = (data-model)/error, with respect to the best-fitting model.

(χ^2/d.o.f. = 826/581). We then replaced the single-temperature blackbody with a multicoloured blackbody (diskbb; Mitsuda et al. 1984) as the thermal component and set the blackbody as the seed (*inp_type* = 0). This provided a slight improvement with χ^2/d.o.f. = 758/581. The fit showed systematic residuals around 7 keV, which hints at the Fe emission line (e.g. Cackett et al. 2009; Papitto et al. 2009; Di Salvo et al. 2019), so we added a Gaussian component to the model. During the fit, we constrained the emission-line energy to be within the 6.4–7.0 keV energy range (corresponding to Fe K emission). We found that the Gaussian line energy pegged at the upper limit of 7 keV with a width broader than 1 keV. So we constrained the Gaussian linewidth to be within 0–1 keV. The addition of this Gaussian component improved the fit significantly to χ^2/d.o.f. ∼ 726.7/579 with an *F*-test probability of improvement by chance ∼5 × 10⁻⁶. The equivalent width of this iron emission-line feature was about ∼0.26 keV, while ∼0.1 keV was observed with the *NuSTAR* observation of the 2015 outburst (Di Salvo et al. 2019). Further, the obtained spectral residuals at low energies hint at some emission feature around 0.9 keV, possibly as a result of an Ne IX or Fe L blend. Similar emission features have been seen with *XMM–Newton* observations (Di Salvo et al. 2019). This encouraged us to add another Gaussian emission-line model. The addition of the emission line at ∼0.85 keV further improved the fit to χ^2/d.o.f. ∼ 700/576 with an F-test probability of improvement by chance ∼9 × 10⁻⁵. The best-fitting 0.5–25 keV persistent spectrum of SAX J1808.4–3658 is shown in Fig. 7 and the best-fitting parameters are listed in Table 4. We also estimated the 0.1–100 keV unabsorbed flux of 1.3 × 10⁻⁹ erg cm⁻² s⁻¹ from the best-fitting model, which translates to X-ray luminosity of 1.9 × 10³⁶ erg s⁻¹ for a distance of 3.5 kpc (Galloway & Cumming 2006). We also tried to change the input seed source to the disc and we obtained similar spectral fit parameters, except for kT_{seed} = 0.57 keV with $\Delta\chi^2$ = +6 for no additional d.o.f.

4 DISCUSSION AND CONCLUSION

SAX J1808.4–3658 was observed in its ninth outburst in 2019. The *AstroSat* observed it for ∼1.5 d near the peak of the outburst. We report results from our broad-band timing and spectral study

Table 4. The best-fitting spectral parameters obtained from the SXT + LAXPC spectrum of SAX J1808.4–3658. Reported errors and limits are at the 90 per cent confidence level for a single parameter. Unabsorbed flux (0.1–100 keV) is in units of erg cm^{-2} s^{-1}. X-ray luminosity is in 0.1–100 keV for a distance of 3.5 kpc.

Model	Parameter	SXT + LAXPC
tbabs	N_H (10^{22} cm^{-2})	0.056 ± 0.007
diskbb	kT_{in} (keV)	$1.08^{+0.03}_{-0.02}$
	Norm	$7.8^{+1.2}_{-1.0}$
nthcomp	Γ	$1.67^{+0.02}_{-0.01}$
	kT_{seed} (keV)	0.322 ± 0.025
	inp_type	0
	kT_e (keV)	100^{fixed}
	Norm (10^{-2})	3.7 ± 0.3
Gaussian 1	E_{Line} (keV)	$7.0^{pegged}_{-0.25}$
	σ (keV)	$1.0^{pegged}_{-0.2}$
	Eqw (keV)	$0.26^{+0.11}_{-0.14}$
	Norm (10^{-4})	7 ± 2
Gaussian 2	E_{Line} (keV)	$0.86^{+0.04}_{-0.07}$
	σ (keV)	$0.08^{+0.05}_{-0.03}$
	Eqw (keV)	0.022 ± 0.010
	Norm (10^{-3})	$2.0^{+1.4}_{-0.8}$
Constant	C_{LAXPC}	1 (fixed)
	C_{SXT}	1.04 ± 0.02
SXT gain	Gain (eV)	34^{+2}_{-4}
Unabsorbed flux	$F_{0.1-100 \, keV}$	1.3×10^{-9}
Luminosity	L_X (erg s^{-1})	1.9×10^{36}
	χ^2/d.o.f.	700/576

of SAX J1808.4–3658 performed using *AstroSat* data. The 0.004–200 Hz PDS showed noise components that can be described by three Lorentzian functions with integrated rms of 17.5 per cent, 11 per cent, and 13 per cent. Moreover, we found coherent X-ray pulsations at ~401 Hz. The pulse timing results obtained are compatible within the errors with the solution obtained with NICER (Bult et al. 2020). The pulse profiles obtained in the energy band 3–20 keV suggest fractional amplitudes of 3.5 per cent, 1.2 per cent, and 0.37 per cent for the fundamental, second and third harmonics, respectively. Using pulse phase delays, we obtained an upper limit (3σ) on the spin-down rate of ~-4×10^{-11} Hz s^{-1} and spin-up rate of ~7×10^{-11} Hz s^{-1} for the duration of the *AstroSat* observation.

We also checked for the dependence of fractional amplitude and phase lag on the energy in the 3–30 keV range. The fractional amplitude and phase lag were found to be energy-dependent, as previously observed (e.g. Hartman et al. 2009; Sanna et al. 2017; Bult et al. 2020). The fundamental component showed fractional amplitude of ~ 5 per cent up to 5 keV, after which it starts decreasing and reaches around 2 per cent. The harmonic component showed an increasing trend in the 3–30 keV energy range from ~ 1 per cent to 2 per cent. A similar trend of increase in the fractional amplitude of the harmonic with energy has been observed in previous outbursts. The energy dependence of the fractional amplitudes varies considerably between different outbursts (e.g. Hartman et al. 2009; Patruno et al. 2009a; Sanna et al. 2017). Also, we did not detect any drop in fractional amplitude in the 6–7 keV energy range (corresponding to the Fe line) as observed in the 2008 and 2015 outbursts (Patruno et al. 2009a; Sanna et al. 2017).

SAX J1808.4–3658 is known to show energy-dependent time lags in which soft X-rays lag hard X-rays, that is, the pulse peaks at a later phase in softer energies (e.g. Cui, Morgan & Titarchuk 1998; Gierliński et al. 2002; Hartman et al. 2009; Ibragimov & Poutanen 2009). We also found a similar trend with the LAXPC. The lag for the fundamental component is soft and increased from 3 to ~10 keV, whereas the harmonic component showed the opposite trend (i.e. hard lags of similar order). The lags of SAX J1808.4–3658 are flux-dependent and increase with a drop in the accretion rate. The soft lags in the fundamental component are observed throughout the outbursts while lags for the harmonic component are less pronounced or become hard lags when source flux is high (Hartman et al. 2009; Ibragimov & Poutanen 2009). These lags can be explained by the model where the soft thermal component and Comptonization emissivity (or beaming) patterns are different, which are affected in a different way by the fast stellar rotation (Gierliński et al. 2002; Poutanen & Gierliński 2003; Ibragimov & Poutanen 2009).

The 0.3–25 keV broad-band spectrum of SAX J1808.4–3658 was well described by the combination of a thermal component as a multicoloured blackbody, Comptonized emission of soft thermal photons and emission lines. A multicoloured disc-like component statistically better fits the soft continuum than a single-temperature blackbody. The thermal emission was found to be of ~1 keV temperature with compact emission size, possibly from an NS or accretion column. The Comptonized emission associated with a hot corona is characterized by a photon index of 1.67. A power-law photon index of 1.89 was measured from *NuSTAR* observation of 2019 at the outburst peak (Sanna et al. 2019). The electron temperature of the corona was unconstrained and the input seed temperature was found to be ~0.3 keV for the blackbody seed and ~0.5 keV for the diskbb seed. This soft component provides the seed photons to the Comptonized medium, which is not directly visible. The best-fitting spectral parameters suggest that the source was in the hard spectral state during the *AstroSat* observation (Table 4). Throughout the outburst, the X-ray spectrum was hard during both the main outburst peak and the reflaring period (Bult et al. 2019b,c; Sanna et al. 2019). The hardness ratio observed from *AstroSat* did not show any significant variations, suggesting that the source was in the same state throughout the observation. Also, no significant variations in the hardness ratio were observed with *Swift*/XRT during the whole outburst of 2019 (Baglio et al. 2020). Therefore, SAX J1808.4–3658 never left the hard state and went directly from a hard-state main outburst to a reflaring state (see, e.g. Patruno et al. 2016; Baglio et al. 2020). During the outburst of 2015, Di Salvo et al. (2019) reported the state transition in SAX J1808.4–3658 with *XMM–Newton* (soft state) and *NuSTAR* (hard state) observations.

Generally, AMXPs show a hard spectrum with n electron temperature of a few tens of keV (Falanga et al. 2005; Gierliński & Poutanen 2005; Papitto et al. 2010, 2013; Wilkinson et al. 2011; Sanna et al. 2018a,b; Di Salvo et al. 2019). Another AMXP, SAX J1748.9–2021, also showed a spectral state transition from a hard to soft state during bright outbursts (Patruno et al. 2009b; Pintore et al. 2016; Li et al. 2018; Sharma et al. 2019, 2020). However, during the fainter outburst where SAX J1748.9–2021 has similar luminosities as SAX J1808.4–3658 (~10^{36}–10^{37} erg s^{-1}), the source seems to stay in the hard state and does not show state transitions (in 't Zand et al. 1999; Sharma et al. 2020). So, AMXPs show hard-spectrum like faint transients when emitting at low luminosities.

ACKNOWLEDGEMENTS

DATA AVAILABILITY

Data used in this work can be accessed through the Indian Space Science Data Center (ISSDC) at https://astrobrowse.issdc.gov.in/astro_archive/archive/Home.jsp.

REFERENCES

Agrawal P. C., 2006, Adv. Space Res., 38, 2989
Ambrosino F. et al., 2021, Nat. Astron., 5, 552
Antia H. M. et al., 2017, ApJS, 231, 10
Arnaud K. A., 1996, in Jacoby G. H., Barnes J., eds, ASP Conf. Ser. Vol. 101, Astronomical Data Analysis Software and Systems V. Astron. Soc. Pac., San Francisco, CA, p. 17
Baglio M. C., Russell D. M., Lewis F., 2019a, The Astronomer's Telegram, 13103, 1
Baglio M. C., Russell D. M., Lewis F., Saikia P., 2019b, The Astronomer's Telegram, 13162, 1
Baglio M. C. et al., 2020, ApJ, 905, 87
Belloni T., Psaltis D., van der Klis M., 2002, ApJ, 572, 392
Bhattacharyya S., Strohmayer T. E., 2007, ApJ, 656, 414
Bult P., van der Klis M., 2015, ApJ, 806, 90
Bult P. et al., 2019a, ApJ, 885, L1
Bult P. M. et al., 2019b, The Astronomer's Telegram, 13001, 1
Bult P. M., Gendreau K. C., Arzoumanian Z., Strohmayer T. E., Chakrabarty D., Jaisawal G. K., Chenevez J., Guver S. G. T., 2019c, The Astronomer's Telegram, 13077, 1
Bult P., Chakrabarty D., Arzoumanian Z., Gendreau K. C., Guillot S., Malacaria C., Ray P. S., Strohmayer T. E., 2020, ApJ, 898, 38
Bult P. et al., 2022, ApJ, 935, L32
Burderi L. et al., 2007, ApJ, 657, 961
Burderi L., Riggio A., di Salvo T., Papitto A., Menna M. T., D'Aì A., Iaria R., 2009, A&A, 496, L17
Cackett E. M., Altamirano D., Patruno A., Miller J. M., Reynolds M., Linares M., Wijnands R., 2009, ApJ, 694, L21
Cackett E. M. et al., 2010, ApJ, 720, 205
Campana S., Di Salvo T., 2018, in Rezzolla L., Pizzochero P., Jones D. I., Rea N., Vidaña I., eds, Astrophysics and Space Science Library Vol. 457,. Springer, Berlin, p. 149
Chakrabarty D., Morgan E. H., 1998, Nature, 394, 346
Charles P., 2011, in Schmidtobreick L., Schreiber M. R., Tappert C., eds, ASP Conf. Ser. Vol. 447, Evolution of Compact Binaries. Astron. Soc. Pac., San Francisco, CA, p. 19
Cornelisse R. et al., 2009, A&A, 495, L1
Cui W., Morgan E. H., Titarchuk L. G., 1998, ApJ, 504, L27
Deeter J. E., Boynton P. E., Pravdo S. H., 1981, ApJ, 247, 1003
Di Salvo T., Sanna A., 2020, preprint (arXiv:2010.09005)
Di Salvo T., Sanna A., Burderi L., Papitto A., Iaria R., Gambino A. F., Riggio A., 2019, MNRAS, 483, 767
Falanga M. et al., 2005, A&A, 444, 15
Gaensler B. M., Stappers B. W., Getts T. J., 1999, ApJ, 522, L117
Galloway D. K., Cumming A., 2006, ApJ, 652, 559
Gendreau K., Arzoumanian Z., 2017, Nat. Astron., 1, 895
Gierliński M., Poutanen J., 2005, MNRAS, 359, 1261
Gierliński M., Done C., Barret D., 2002, MNRAS, 331, 141
Goodwin A. J., Russell D. M., Galloway D. K., in't Zand J. J. M., Heinke C., Lewis F., Baglio M. C., 2019, The Astronomer's Telegram, 12993, 1
Goodwin A. J. et al., 2020, MNRAS, 498, 3429
Hartman J. M. et al., 2008, ApJ, 675, 1468
Hartman J. M., Patruno A., Chakrabarty D., Markwardt C. B., Morgan E. H., van der Klis M., Wijnands R., 2009, ApJ, 702, 1673
Hasinger G., van der Klis M., 1989, A&A, 225, 79
Heinke C. O., Jonker P. G., Wijnands R., Deloye C. J., Taam R. E., 2009, ApJ, 691, 1035
Ibragimov A., Poutanen J., 2009, MNRAS, 400, 492
in 't Zand J. J. M., Heise J., Muller J. M., Bazzano A., Cocchi M., Natalucci L., Ubertini P., 1998, A&A, 331, L25
in 't Zand J. J. M. et al., 1999, A&A, 345, 100
Jain C., Dutta A., Paul B., 2007, Journal of Astrophysics and Astronomy, 28, 197
Li Z. et al., 2018, A&A, 620, A114
Ludlam R. M., Miller J. M., Degenaar N., Sanna A., Cackett E. M., Altamirano D., King A. L., 2017, ApJ, 847, 135
Mitsuda K. et al., 1984, PASJ, 36, 741
Mukherjee D., Bult P., van der Klis M., Bhattacharya D., 2015, MNRAS, 452, 3994
Ng M. et al., 2021, ApJ, 908, L15
Nowak M. A., 2000, MNRAS, 318, 361
Pan Y. Y., Zhang C. M., Song L. M., Wang N., Li D., Yang Y. Y., 2018, MNRAS, 480, 692
Papitto A., Di Salvo T., D'Aì A., Iaria R., Burderi L., Riggio A., Menna M. T., Robba N. R., 2009, A&A, 493, L39
Papitto A., Riggio A., di Salvo T., Burderi L., D'Aì A., Iaria R., Bozzo E., Menna M. T., 2010, MNRAS, 407, 2575
Papitto A. et al., 2013, MNRAS, 429, 3411
Parikh A. S., Wijnands R., 2019, The Astronomer's Telegram, 13000, 1
Patruno A., Watts A. L., 2012, preprint (arXiv:1206.2727)
Patruno A., Rea N., Altamirano D., Linares M., Wijnands R., van der Klis M., 2009a, MNRAS, 396, L51
Patruno A., Altamirano D., Hessels J. W. T., Casella P., Wijnands R., van der Klis M., 2009b, ApJ, 690, 1856
Patruno A., Watts A., Klein Wolt M., Wijnands R., van der Klis M., 2009c, ApJ, 707, 1296
Patruno A., Maitra D., Curran P. A., D'Angelo C., Fridriksson J. K., Russell D. M., Middleton M., Wijnands R., 2016, ApJ, 817, 100
Patruno A. et al., 2017, ApJ, 841, 98
Pintore F. et al., 2016, MNRAS, 457, 2988
Poutanen J., Gierliński M., 2003, MNRAS, 343, 1301
Russell D. M., Goodwin A. J., Galloway D. K., in't Zand J. J. M., Lewis F., Baglio M. C., 2019, The Astronomer's Telegram, 12964, 1
Sanna A. et al., 2017, MNRAS, 471, 463
Sanna A. et al., 2018a, MNRAS, 481, 1658
Sanna A. et al., 2018b, A&A, 610, L2
Sanna A., Di Salvo T., Burderi L., Riggio A., Gambino A., Iaria R., 2019, The Astronomer's Telegram, 13022, 1
Sanna A. et al., 2020, MNRAS, 495, 1641
Sanna A. et al., 2022a, MNRAS, 514, 4385
Sanna A. et al., 2022b, MNRAS, 516, L76
Sanna A. et al., 2022c, The Astronomer's Telegram, 15559, 1
Sharma R., Jain C., Dutta A., 2019, MNRAS, 482, 1634
Sharma R., Beri A., Sanna A., Dutta A., 2020, MNRAS, 492, 4361
Sharma R., Jain C., Rikame K., Paul B., 2023, MNRAS, 519, 1764
Singh K. P. et al., 2014, Proc. SPIE, 9144, 91441S
Singh K. P. et al., 2016, Proc. SPIE, 9905, 99051E

Singh K. P. et al., 2017, Journal of Astrophysics and Astronomy, 38, 29
Tudor V. et al., 2017, MNRAS, 470, 324
van der Klis M., 2004, preprint (astro-ph/0410551)
van Straaten S., van der Klis M., Wijnands R., 2005, ApJ, 619, 455
Wang Z. et al., 2001, ApJ, 563, L61
Wang Z., Breton R. P., Heinke C. O., Deloye C. J., Zhong J., 2013, ApJ, 765, 151
Wijnands R., van der Klis M., 1998a, Nature, 394, 344
Wijnands R., van der Klis M., 1998b, ApJ, 507, L63
Wijnands R., van der Klis M., Homan J., Chakrabarty D., Markwardt C. B., Morgan E. H., 2003, Nature, 424, 44
Wilkinson T., Patruno A., Watts A., Uttley P., 2011, MNRAS, 410, 1513
Wilms J., Allen A., McCray R., 2000, ApJ, 542, 914
Yadav J. S. et al., 2016, Proc. SPIE, 9905, 99051D
Zdziarski A. A., Johnson W. N., Magdziarz P., 1996, MNRAS, 283, 193
Życki P. T., Done C., Smith D. A., 1999, MNRAS, 309, 561

APPENDIX A: ENERGY-RESOLVED PULSE PROFILES
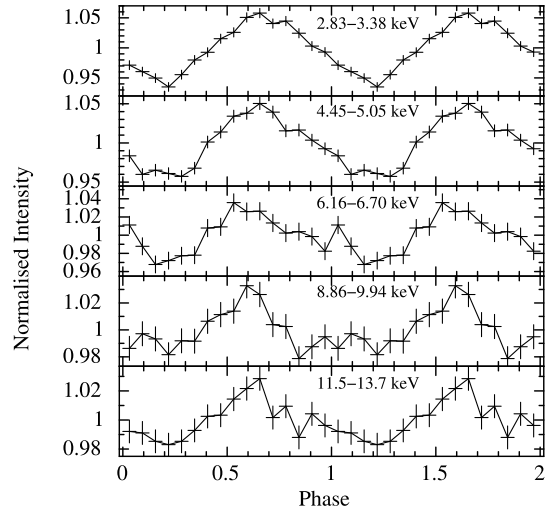
Figure A1. Energy-resolved pulse profiles of SAX J1808.4–3658. The energy range used is given in each panel.

This paper has been typeset from a TEX/LATEX file prepared by the author.